Multi-Channel Synthetic Aperture Radar Based Classification of Maritime Scenes

ROBERT W. JANSEN[1], (Member, IEEE), **MARK A. SLETTEN**[1], (Senior Member, IEEE),
THOMAS L. AINSWORTH[1], (Fellow, IEEE), AND **RAGHU G. RAJ**[2], (Senior Member, IEEE)

[1]Remote Sensing Division, U.S. Naval Research Laboratory, Washington, DC 20375, USA
[2]Radar Division, U.S. Naval Research Laboratory, Washington, DC 20375, USA

Corresponding author: Robert W. Jansen (bob.jansen@nrl.navy.mil)

ABSTRACT We present novel experimental evidence that demonstrates the effectiveness of exploiting scene motion information for the analysis of scene structure in maritime imaging applications. We analyze data captured by our novel airborne Multi-channel SAR (MSAR) system that is particularly suited to sampling the velocity profile of scatterers in the maritime environment. While previous works have shown the utility MSAR systems for correcting scene motion induced blurring artifacts, our work shows, for the first time, how the information furnished by an MSAR system can systematically render accurate classification of maritime scenes into different perceptual categories. We offer a methodology that is superior to traditional classification techniques that are based purely on the spatial structure of an image. Furthermore, the simplicity of the feature space involved together with the demonstrated classification performance on imagery captured by our airborne MSAR system underscore the strength of the methodology.

INDEX TERMS Multi-channel synthetic aperture radar (SAR), ocean imaging, image classification.

I. INTRODUCTION

Two well-known issues in SAR imaging are the displacement and blurring effects caused by uncompensated motion of either the platform or the scene [1], [2]. While the effects of platform motion can be compensated using information gathered from inertial navigation units, scene motion is largely handled, in single phase center SAR systems, by employing blind deblurring algorithms that exploit statistical and physics-based models to capture spatially varying motion signatures, with varying degrees of success [3], [4]. The deleterious effects of scene motion (on the quality of SAR image formation) is particularly accentuated in maritime imaging applications where virtually every scatterer in the scene undergoes motion governed by complex physical processes that are difficult to characterize. In such cases, traditional approaches to scene induced motion compensation are known to be inadequate [5]. Recently, Multi-channel SAR (MSAR) imaging has been demonstrated as a powerful approach to systematically ameliorating the aforementioned scene induced motion error problem [5]–[10]. In particular, the additional along-track receivers provide new, independent

information about the scene that can be used to correct automatically for the underlying scene motion.

Based on this foundation, we address a fundamental question as to whether the in-scene motion information derived from an MSAR with along-track phase centers can be effectively exploited to extract higher-level perceptual information–in particular to perform scene classification. And, if so, can generic MSAR parameters be found that provide useful, interpretable characterization of the in-scene motions?

We answer these questions by demonstrating, for the first time, an efficient and flexible classification algorithm that utilizes the in-scene MSAR-derived motion information. This method complements existing approaches to classification [11]–[19] and image segmentation [20]–[27] that exploit the spatial structure of static amplitude images. Our experimental results, performed on imagery captured by the U.S. Naval Research Laboratory (NRL) airborne MSAR system [5], [8], [9], demonstrate how the motion information furnished by an MSAR system can be systematically used to enhance maritime scene classification in a manner that is superior to purely amplitude-based approaches.

The MSAR airborne system operates at X-band with a center frequency of 9.875 GHz and uses linear frequency

modulated chirped waveforms with a bandwidth of 220 MHz to achieve a range resolution of approximately 0.7 m. The peak radiated power is approximately 1.4 kW, while the aggregate pulse repetition frequency (PRF) of 25 kHz and pulse length of 6 μs produced an average power of 210 W. The system flies on a Saab 340 aircraft using a belly-mounted radome with a nominal incidence angle of 70°. Typical altitude and airspeeds are 914 m (3000 ft) and 70 m/s, respectively. The system use a linear array of 16 receive antennas with a transmit horn located at each end. During each pair of pulse intervals (one for each horn), four of the 16 receive antennas are connected to a four-channel receiver and sampled by a high-speed data recorder. After each pair of pulses, a bank of microwave switches is reconfigured to connect the next group of four receive antennas to the receiver and data recorder. In this manner, 32 phase centers are generated, one corresponding to each combination of transmit and receive antennas, and each are sampled at a rate of 3.125 kHz. This is sufficient to allow production of 32 SAR images, one corresponding to each phase center, that are free from azimuthal ambiguities.Further details of our MSAR system and its performance are given in [8].

Our new classification approach aims to identify targets and surface features through differences in the number and velocity of their scattering centers. Employing data from an MSAR system that supports M along-track phase centers, we construct an $M \times M$ covariance matrix at each pixel to quantify the complex (i.e. magnitude and phase) correlations amongst the M signals. These correlations promise to be very useful target/clutter discriminators. As with many classification schemes such as SAR polarimetry [28], eigen analysis of this covariance matrix serves as the basis of our approach. We derive new classification parameters from the obtained eigenvalues and eigenvectors. Our empirical results indicate that the entropy of the covariance matrix, coefficients and phases of the eigenvector components, and eigenvalue spectrum provide a basis for maritime scene characterization.

The novelty of our approach stems from the inclusion of motion information, rather than purely amplitude and amplitude texture information, for scene classification. Our covariance matrix is unique in that it correlates the returns from multiple along-track channels. Additionally, apart from improving image quality, the MSAR processing corrects both motion distortions and motion-induced displacements, which improves the coherence of our covariance matrix [8].

We provide the first demonstration of this technique using our airborne NRL MSAR dataset that was captured with multiple along-track phase centers. The approach shown here can be easily extended to an MSAR system that supports both along-track and cross-track phase centers which would produce data with a covariance matrix rich with information on both motion and height. It is anticipated that this will allow even better classification of the dynamic sea surface in addition to the vessels that ride on it.

The rest of this paper is organized as follows. In Section II, we provide a detailed description of our classification methodology that forms the basis of our image classification algorithm. Sections III and IV develop the MSAR features used for classification and the classification algorithm employed. In Section V, we demonstrate the performance of our maritime scene analysis algorithm applied to the NRL MSAR datasets. Finally, we conclude in Section VI with a summary of our results together with directions for future research.

II. METHODOLOGY
Our scene classification methodology takes advantage of the motion characteristics of maritime scenes. The classes of interest (vessels, ambient water, etc.) all have time dependent characteristics that are exploitable by the unique motion-sensing properties of the MSAR system.

A. MOTION RELATED POSITION CORRECTION
The displacement effect in SAR imagery is described by the well-known Doppler shift δ_a[4]

$$\delta_a = R * V_r / V_p \qquad (1)$$

where R is the range from platform to target, V_r is the target range speed, and V_p is the SAR platform speed. The motions associated with a scatterer results in a spatial spreading and shifting of the target signature within the image. Therefore a purely spatial analysis of the image will not allow an accurate inference of the time varying motions associated with each scatterer comprising the scene. The first step is to reposition target signatures back to their true location in the image. We utilize MSAR's imagery from multiple along-track phase centers to correct motion-induced displacements. These position corrections can be achieved using methods such as Velocity SAR (VSAR) [5]–[10] or Along-Track Interferometry (ATI) [5], [29]. Here we use the VSAR algorithm which repositions all of the backscatter generated from a given target, regardless of its associated Doppler velocity and displacement, to a more compact, corrected position. The VSAR procedure has been extensively described elsewhere [5]–[10], although here we retain the complex pixels throughout. Specifically our VSAR processing steps are 1) Form image stack using each of the M phase center images. 2) Perform the FFT for each pixel along the time stack. 3) Shift each velocity component back to the origin in order to enforce stationarity, 4) Trim edges to remove non-overlapping portions. The VSAR-based repositioning of target backscatter returns to the appropriate complex image pixel positions allows coherent analysis of target motion via eigen analysis of the $M \times M$ covariance matrix.

B. COVARIANCE MATRIX
To capture motion information at each pixel, (i, j), we start by constructing the covariance array for all phase-center pairs (m, n):

$$C_{ijmn} = <I_{ijm}I_{ijn}^*> . \qquad (2)$$

The spatial averaging implied in (2) is over a window smaller than the smallest targets of interest. In practice, we use a 5×5 pixel window for spatial averaging in (2). For practical purposes, we subsequently subsample to half the smoothing window size to reduce final pixel dimensions. At each pixel, (i, j) we generate the M eigenvalues λ_m and eigenvectors $\overrightarrow{v_m}(m = 1 \text{ to } M)$ of the covariance matrix C

$$C\overrightarrow{v_m} = \lambda_m \overrightarrow{v_m} \qquad (3)$$

for use in our classification procedure. We dropped the (i, j) indices for brevity. The eigenvalues and eigenvectors characterize the in-scene motions at each pixel throughout the MSAR collection time.

C. POINT TARGET VELOCITY ANALYSIS

After VSAR processing, the set of MSAR images, each spatially co-located but offset in time, form an along-track interferometric image stack. The phase differences between pairs of images in the stack provide estimates of the average radial displacement of the dominant scatterers for a given pixel. The phase difference depends on the time difference between the pair of images, the average velocity of the dominant scatterers, and the imaging geometry, i.e. look direction and incidence angle. The imaging geometry and in-scene scatterer velocity determine the radial velocity, v_{radial}, of the scatterer toward, or away from, the radar. Therefore, the radial displacement of the scatterer, Δd, is $v_{radial} \cdot \Delta t$, where Δt is the time difference between the interferometric pair. The absolute along-track interferometric phase difference is then

$$\Delta\phi_{abs.} = 2 \cdot \Delta d / w = \left(2 \cdot \Delta t / w \right) v_{radial} \qquad (4)$$

where w is the radar wavelength. The observed phase difference, $\Delta\phi_{obs.}$, lies within the range $[0, 2\pi]$. Therefore,

$$\Delta\phi_{obs.} = \Delta\phi_{abs.} + (2\pi n) \qquad (5)$$

where n is an integer. For a point scatterer moving at constant velocity, the observed phase difference, $\Delta\phi_{obs.}$ (modulo 2π), and time difference, Δt, will generate the same radial velocity, v_{radial}, independent of the pair of images chosen from the stack. Therefore, at each pixel, the phases of the interferometric image stack advance linearly in time. This, of course, assumes that the scattering does not significantly de-correlate during the imaging time and that the imaging geometry remains relatively fixed.

For the specific case of our MSAR images, the time difference between adjacent images is fixed, $\Delta t \sim 0.001$ seconds, as is the radar wavelength, $w \sim 3$ centimeters. For a pixel containing a coherent, dominant scatterer, the MSAR image stack will be proportional to

$$S \propto \left[1, e^{i\Delta\phi}, e^{i2\Delta\phi}, e^{i3\Delta\phi}, \dots, e^{i(M-1)\Delta\phi} \right] \qquad (6)$$

using M images, and the resulting covariance matrix is then

$$C = S^{\dagger} \cdot S \propto \begin{bmatrix} 1 & e^{i\Delta\phi} & \cdots & e^{i(M-1)\Delta\phi} \\ e^{-i\Delta\phi} & 1 & & \vdots \\ \vdots & & \ddots & \\ e^{-i(M-1)\Delta\phi} & \cdots & & 1 \end{bmatrix} \qquad (7)$$

where $S^{\dagger}$ is the Hermitian conjugate of S.

Eigen analysis of this covariance matrix identifies a single large eigenvalue and its associated eigenvector. By inspection, the associated eigenvector of the rank-1 matrix in (7) is proportional to $\left[1, e^{-i\Delta\phi}, \dots, e^{-i(M-1)\Delta\phi} \right]$. The phases of the eigenvector components are determined directly from the phases of MSAR images; they progress linearly from the first to the last component. This is the ideal case for a rank-1 covariance matrix with no spatial decorrelation. In practice, we find that the covariance matrices are often nearly rank-1. The secondary eigenvalues are much weaker than the primary eigenvalue and thus the secondary eigenvectors do not affect the analysis of the dominant eigenvector. However, if there is no dominant scatterer, or the scattering decorrelates, or the in-scene motion is not uniform, then the phases of the eigenvector components become random and the in-scene scatterer velocities are not retrieved by eigen analysis.

The sum of all eigenvalues, λ_m, at a given pixel is the total power backscattered by the full set of MSAR images averaged over the 5×5 window mentioned in Section II.B. For a rank-1 covariance matrix, only the first eigenvalue, λ_1, is non-zero. As the rank of the covariance matrix increases, additional eigenvalues become non-zero. However, in many cases we find that the eigenvalue spectrum rapidly decays, i.e. $\lambda_1 \gg \lambda_2 \gg \lambda_3 \gg \lambda_4 \cdots \lambda_M \sim 0$.

III. FEATURE EXTRACTION: PRELIMINARY OBSERVATIONS

Given the phase history data received at the various phase centers of the MSAR system, we form a complex image for each phase center using a chirp-scale algorithm (though in general, any SAR imaging algorithm, such as backprojection, can be used). The VSAR processing then corrects this image stack, repositioning the targets to their actual in-scene locations. The VSAR procedure has been presented previously [5]–[10], however in the method presented here we perform the VSAR correction retaining the coherent, complex data for each channel. This allows the $M \times M$ covariance matrix of the VSAR corrected image pairs to characterize the in-scene motions observed by the MSAR system. After the spatial averaging mentioned in Section II.B, eigen analysis of the covariance matrices generates the eigenvalues λ_m and eigenvectors $\overrightarrow{v_m}(m = 1 \text{ to } M)$, as in (2)–(3).

To motivate our feature extraction approach, we consider the sample image in Fig. 1 where we examine a region, highlighted by the yellow box, of an MSAR dataset collected using the NRL airborne MSAR system) that contains identifiable ambient water, surf, boats and their wakes, beach and land. The system collected 32 MSAR phase centers,
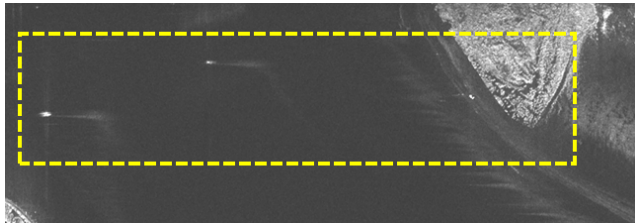
FIGURE 1. The highlighted region of this MSAR dataset is used for classification validation. The region contains areas of ambient water, land, beach, surf, boat and their wakes.

here we use $M = 8$ of the phase centers for our analysis. Preliminary testing showed that higher M was not necessary for our purposes here (although our analysis is extensible to any arbitrary number of phase centers).

The key idea is to perform an eigen analysis of the multichannel covariance matrix associated with each scatterer in the image. This is indeed a novel idea in the realm of multichannel processing which was inspired by earlier works in polarimetric analysis of SAR images [28]. The explicit form the boxcar averaged covariance matrices that we employ is given by:

$$C_{m,n}^{i,j} = \sum_{k=-\Delta_x}^{\Delta_x} \sum_{l=-\Delta_y}^{\Delta_y} C_{i-k,j-l;m,n} \qquad (8)$$

where Δ_x, Δ_y are the local spatial windows along the respective image axes, and $C_{i-k,j-k;mn}$ are the rank-1 covariance matrix from (2). The calculation in (8) serves the two-fold purpose of reducing image speckle and increasing the rank of the covariance matrix, $C_{m,n}^{i,j}$, by aggregating motion information in a localized neighborhood of each pixel. The resulting eigenvalues and eigenvectors, as shown in Fig. 2 and Fig 3, reveal valuable information relating to the signature motion characteristics of the classes of interest.

A. CLASS EIGENVALUES

Fig. 2 shows plots of the normalized eigenvalue means and standard deviations for 5×5 pixel boxes in the image within six different classes - ambient water, surf, boat, wake, land and beach areas. (Specific class regions are identified on the image in Fig. 6.) Fig. 2 shows individual eigenvalues normalized by the sum all eight eigenvalues, i.e. $\lambda_i = \hat{\lambda}_i / \sum_j \hat{\lambda}_j$, where $\hat{\lambda}_i$ are the eigenvalues calculated from the averaged covariance matrix. Overall the eigenvalues beyond the 2nd or 3rd are greatly reduced in magnitude for most classes. The ambient water class is an exception; the eigenvalue spectrum falls off slowly and the normalized dominant eigenvalue is only about 0.4 owing to a more uniform distribution of velocities. On the opposite extreme we see that the stationary land region has almost all of its energy in a single dominant component with a small standard deviation. The other classes have eigenvalue distributions somewhere between these two extremes. Both the plot shapes and the standard deviations vary sufficiently to be useful as part of a classification feature.

B. CLASS EIGENVECTORS

In Fig. 3 we plot the phases associated with the dominant eigenvector components and their standard deviation for 5×5 pixel boxes in the image within six different classes - ambient water, surf, boat, wake, land and beach areas. Overall we see that the complex phases of the eigenvector components for most of the classes are centered about zero. For ambient water the complex phases vary widely (large error bars) owing to non-uniform motion from pixel to pixel and to the signal strength (RCS) approaching the noise floor. The tight error bars of the land and boat phases imply that both display well-defined, uniform motion throughout the MSAR collection interval. For the boat, we find that the phases of the eigenvector components are tightly centered along a slope consistent with the theoretical discussion in Section II.C. Only the boat shows a non-zero velocity; the land is not in motion. The remaining classes, i.e. surf, wake and beach, display phase results intermediate between ambient water and land/boat classes.

An important subtlety here is that amplitude and velocity information may be correlated. Consider the ambient water class, which has both low backscatter amplitudes and surface motions random in speed and direction. Eigen analysis separately addresses these effects. As the backscatter amplitude approaches the system noise floor the covariance matrix decorrelates generating random phases. If the backscatter is significant, i.e. above the noise floor, then the random motion of the water surface decorrelates the covariance matrix. In either case, the covariance matrix analysis retrieves uncorrelated motions, i.e. large phase error bars consistent with zero velocity. Indeed, spatial SAR amplitude information, e.g. low backscatter, has traditionally been exploited for SAR image classification of ambient water. However, boat wakes appear brighter than ambient water, but they still decorrelate due to random surface motion. Conversely, the backscatter from a small boat may blend into the returns from a rougher sea. In this case, the boat may be detected due to its coherent motion, rather than its backscattering amplitude. The point is that amplitude and velocity information may be correlated for a given class, but in different imaging scenarios and for different classes the correlations change.

Our MSAR based analysis enables motion-based discriminatory information to be elicited from the data, which provides target class separation measures complementary to the standard amplitude information. This motion information augments amplitude-based feature sets, providing new information with which to classify SAR imagery. MSAR based analysis, as will be demonstrated below, provides robust classification performance over a range of target classes, employing a richer set of features.

IV. MSAR BASED CLASSIFICATION ALGORITHM

Using the concepts and insights described in previous sections, in this section we describe our MSAR based classification algorithm that makes judicious use of the discriminatory information embedded in the MSAR covariance matrix.
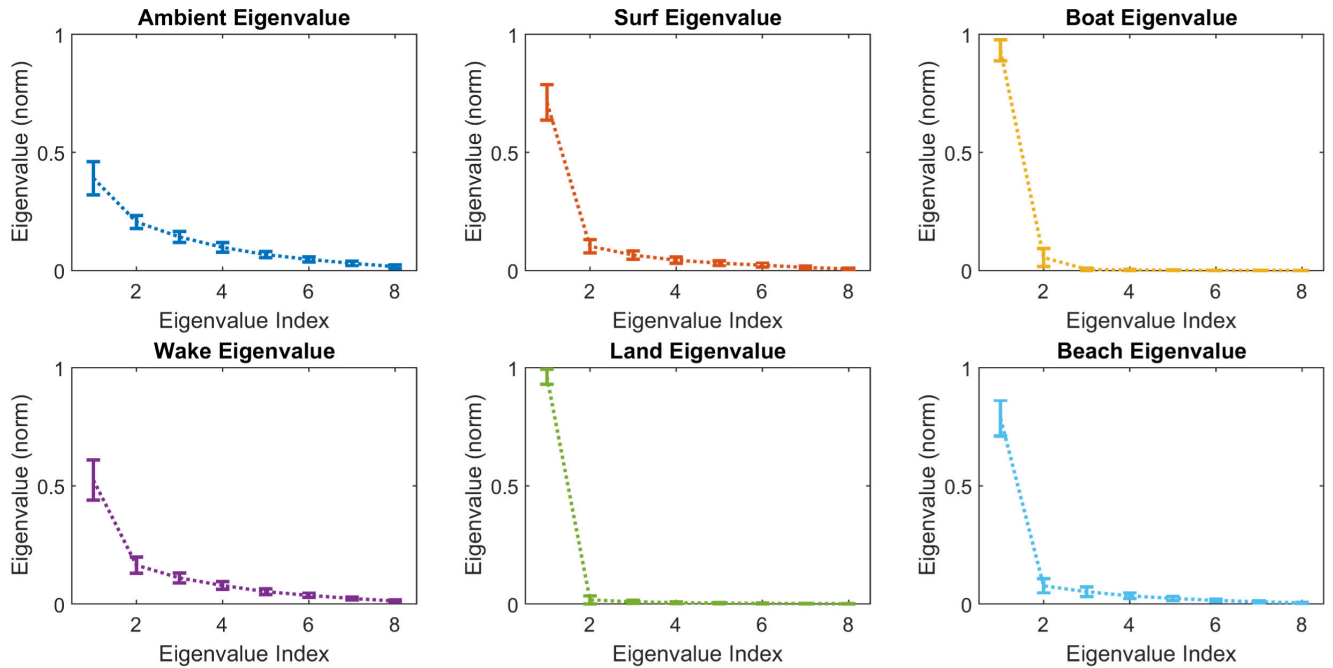
FIGURE 2. Eigenvalue spectrums for the six classes in the MSAR image. Shown are the means and standard deviations of eigenvalues averaged over the highlighted areas in Fig. 6.
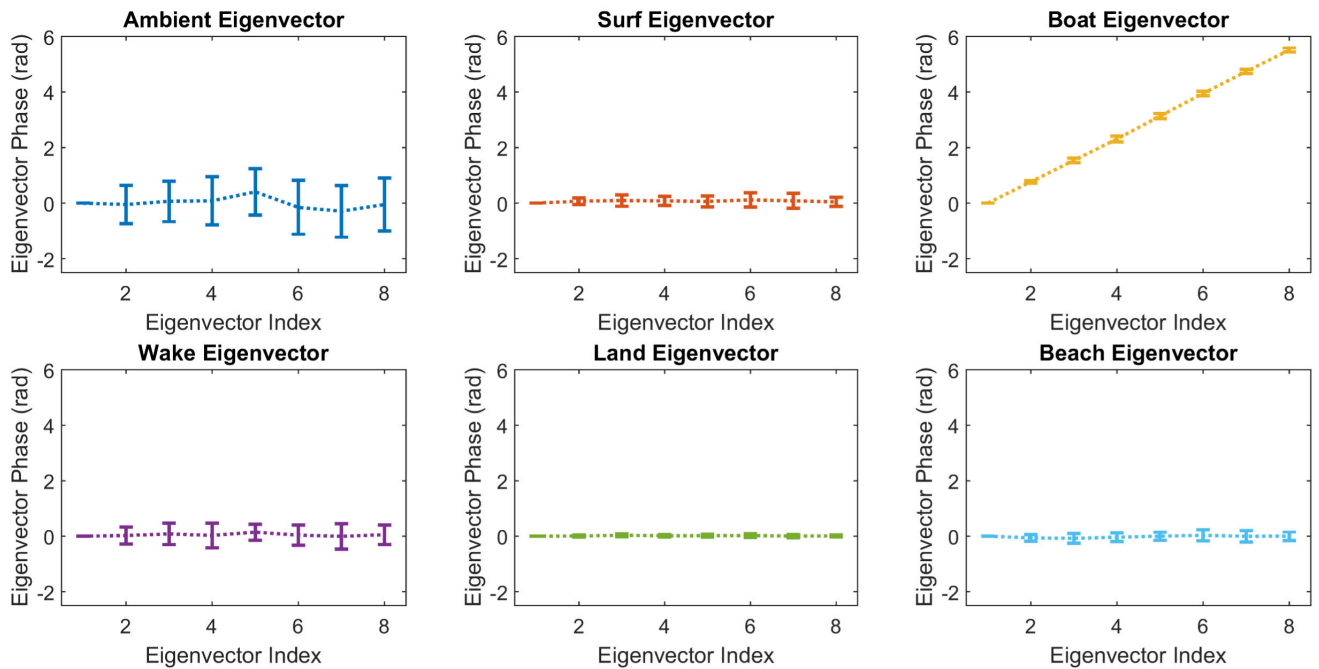

FIGURE 3. Means and standard deviations of the phases of the first (dominant) eigenvector components.

A. CLASSIFICATION ALGORITHM FLOW CHART

The overall flow chart of our algorithm is shown in Fig. 4. Steps 1 and 2 of the flowchart describe the MSAR image formation process that we described in Section II. Steps 3 and 4 of the flowchart describe the key steps of constructing the MSAR covariance matrix and eigenvalue/eigenvector extraction described in Section III. In this section we fully delve into step 5 of the flowchart that involves the critical steps of

feature extraction, from the underlying eigen-structure of the MSAR covariance matrix, followed by classification of the scene pixels.

B. CLASSIFICATION FEATURE CONSTRUCTION

We employ a judicious use of eigenvectors and eigenvalues described in Section III to construct the feature maps that emphasize class characteristics. The simplest and most
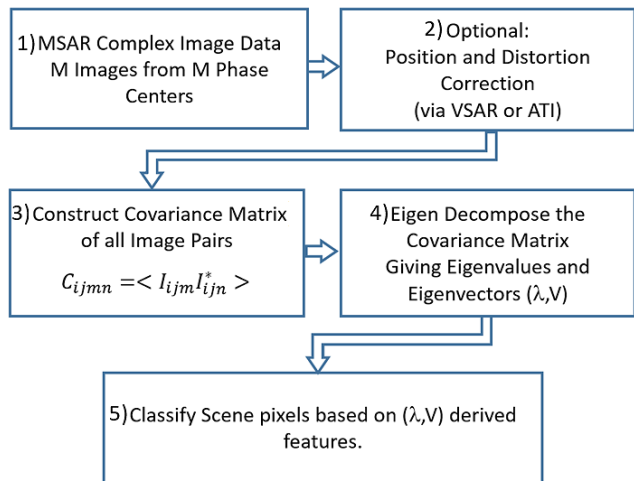
FIGURE 4. Flow chart of MSAR-based classification procedure.

FIGURE 5. Byte-scaled feature maps of the 10 features described in Section IV.

straightforward idea is to directly input all eigenvalues and eigenvectors into a classification algorithm and thereby put the entire burden of finding useful class separations solely on the classifier model. A more directed method is to construct mappings derived from the eigen components that bring out certain desired class features. By iteratively reducing the number of features, we find that to build a robust classifier it suffices (and is desirable) to limit ourselves to the largest eigenvalues and associated eigenvectors. The other eigen-parameters either add undesirable noise or have no useful effect on confidence measures computed by the classification model. We normalized the eigenvalues and concentrated on the phases of the eigenvector components, since the phases relate directly to in-scene motion typical of maritime scenes. Guided by analysis such as that in Section III, we construct eigen-feature maps to differentiate amongst the desired classes. These mappings were culled from over 30 initial features by removing features that did not significantly contribute to classification quality via a Sequential Backward Selection (SBS) procedure [30]. They can be categorized into eigen-derived features (shown in Fig. 5) that characterize different degrees of randomness in motion, spatial uniformity and speeds.

After the SBS we arrived at six features directly related to the largest eigenvalues and properties of their associated eigenvectors at each pixel. The eigenvalue parameters provide the spectral characterization of the covariance matrix. Since only the first few eigenvalues differ significantly from zero, they and their associated eigenvectors are all that is needed to describe the covariance matrix. The information culled from the eigenvectors relates directly to in-scene motion, i.e. the phases and phase coherence of the eigenvectors components. Finally, in order to capture local spatial variations another four features are derived from local spatial standard deviations. These spatial variations are reminiscent of the coefficient of variation often used in SAR amplitude-based classifications.
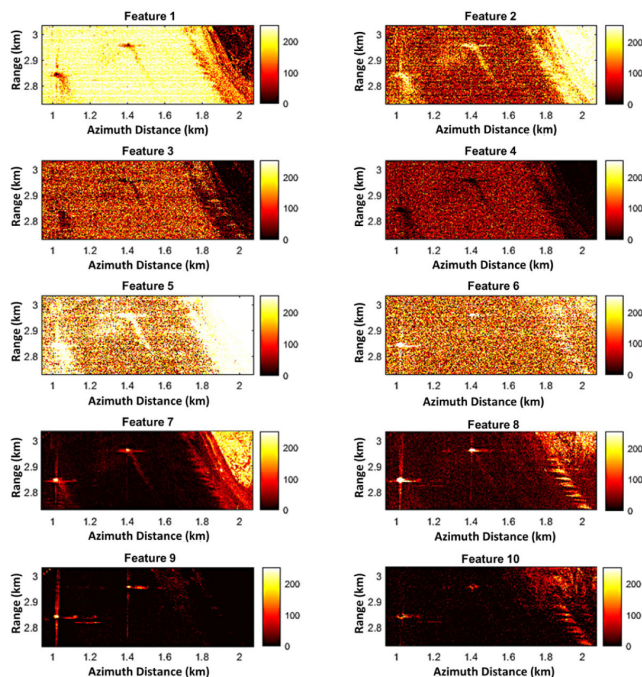
From our experimental design process we distilled the following set of ten features. Keeping more features does not produce better confidences or classifications, whilst removing additional ones shows rapid degradation of classification quality. However we point out that the selected features are not necessarily unique; alternative feature sets may produce similar results provided that the new feature set captures the same information. We relegate more detailed investigations along these lines to future work.

In this paper, our aim is to provide a demonstration of the classification potential of such MSAR-based velocity information, not necessarily an ultimate or unique set of features. We now outline each feature used in more detail. In particular, the following list presents the equations used for our MSAR eigenvalues and eigenvector based classification method:

1) FEATURE 1-ENTROPY
Characterization of the eigenvalue spectrum can be accomplished via the (von Neumann) entropy

$$F_1 = -\sum_{m=1}^{M} \lambda_m \ln \lambda_m \qquad (9)$$

Entropy is related to the distribution of eigenvalues, λ_m, and is a measure of the number and randomness of significant scatterers. For example in ambient regions, we expect distributed scatterers rather than a single dominant scatterer leading to high entropy. Uniform local motion (e.g. ship, land) will have a dominant eigen component and low entropy. The entropy provides an overall, average description of the eigenvalue spectrum.

2) FEATURE 2 TO 4-EIGENVALUE DIFFERENCES

The shape of the eigenvalue spectrum is also a useful characteristic of the motion. This measure is somewhat related to the entropy but more focused on the number of significant scatterers, i.e. the strengths of the dominant and secondary components, and the thus the rapidity of the spectral decay. We found that the largest three eigenvalues ($m = 1, 2, 3$) characterize the eigenvalue spectrum; the remaining are mostly noise, i.e. close to zero. We normalize as follows to remove some scene amplitude dependencies included in the first eigenvalue (see the discussion in Section II.C):

$$F_{2,3,4} = (\lambda_m - \lambda_{m+1})/\lambda_1, \quad m = 1 \text{ to } 3 \tag{10}$$

3) FEATURES 5 TO 6-EIGENVECTOR COHERENCE

If the speed of the target is uniform over the collection time then the images collected by the along-track apertures will differ only by a phase; for evenly spaced apertures the phase difference between adjacent apertures will be a single constant. The coherence across elements of an eigenvector is related to the uniformity of the speed over the entire collection interval. Again, we consider the vector elements, labeled by k, only for the first two eigenvectors ($m = 1, 2$) since these relate most directly to target motion. Eigenvector coherences will be high for classes such as land, boats, and regions of uniform surf. Ambient water and wakes do not display strong phase coherence across the components of the eigenvectors.

$$F_{5,6} = \frac{\left| \sum_{k=1}^{M-1} v_{k,m} v_{k+1,m}^* \right|}{\sum_{k=1}^{M-1} \left| v_{k,m} v_{k+1,m}^* \right|}, \quad m = 1 \text{ to } 2 \tag{11}$$

4) FEATURES 7 TO 8-LOCAL EIGENVALUE VARIATION

Local (spatial) standard deviations of the eigenvalues for the first two eigen components highlight information similar to the coefficient of variation for amplitude-based classification. As explained above, this captures information about the surrounding region uniformity or texture.

$$F_{7,8} = \sqrt{\frac{1}{n} \sum_{ij}^{n} (\lambda_{ij,m} - \xi_m)^2}, \quad m = 1 \text{ to } 2 \tag{12}$$

where the summation over ij is over the n pixels of a small window centered at the pixel of interest, and ξ_m is the mean of λ_m using the same averaging window.

5) FEATURES 9 TO 10-EIGENVECTOR PHASE SLOPE

As described in Section II.C and shown in Fig. 3, the eigenvector phase slope (related to velocity) discriminates between some classes. To capture this information we derive features using the local average phase slope divided by the local average standard deviation of the phase slope. This feature will be higher for moving targets such as boats where the dominant and secondary scatterers are coupled by the boat's motion.

$$F_{9,10} = \left| \frac{S_m}{D_m} \right|, \quad m = 1, 2 \tag{13}$$

Here S_m and D_m are the local (spatial) mean and standard deviation of the phase differences between adjacent eigenvector components, $\Delta_k = \phi_k - \phi_{k+1}$,.

$$S_m = \frac{1}{n(M-1)} \sum_{ij}^{n} \sum_{k=1}^{M-1} \Delta_{ij,k,m}, \tag{14}$$

$$D_m = \frac{1}{n(M-1)} \sqrt{\sum_{ij}^{n} \sum_{k=1}^{M-1} \left(\Delta_{ij,k,m} - S_m \right)^2}, \tag{15}$$

calculated over a small window centered at the pixel of interest.

C. CLASSIFICATION PROCESSING DESCRIPTION

In this paper, we use supervised classification with 6 classes (ambient, surf, boat, wake, beach, and land). Training data is derived from small sections of the scene appropriate for each class. This training data is fed into Support Vector Machine (SVM) classifiers [17] to derive classification models. Among the several possible non-linear SVM models [17], in our experiments we found the simple linear SVM model to be sufficient for furnishing robust and consistent results. The model is then applied to the entire scene to arrive at the class map. It is important to note that our methodology works equally well with other classification schemes and is not limited to the use of SVMs.

Our experimental results below show that our algorithm delivers much improved classification performance on data captured by the NRL MSAR system. We expect better results could be possible with the inclusion of height information provided by adding a cross-track component to the MSAR system (as proposed in future collections).

V. EXPERIMENTAL RESULTS

In this section we demonstrate the performance of our proposed MSAR-based classification method for the MSAR data region shown in Fig. 1. The overall procedure follows the flow chart in Fig. 4. The classification procedure employs a straightforward supervised classification scheme with a linear SVM model. Ground truth is derived from both in situ observations [8] and precise geo-registration of the MSAR imagery to optical Google Earth images.

A. GENERATE FEATURES

The feature maps used in the classification procedure were generated from the eigenvalues and eigenvectors at each pixel using the equations given in Section IV.B. The 10 feature maps are shown in Fig. 5.

We see the entropy map (Fig. 5, Feature 1) is bright in ambient regions where there are a large number of weak scatters and motion is random. Features 2-4 shown in Fig. 5 are eigenvalue differences which are bright in higher motion regions (boat, wake, surf), but already much reduced by the third eigenvalue difference. Features 5 and 6 from Fig. 5 show the eigenvector coherence for the first two eigenvectors, which are bright on land and boat regions. Again, these fall off rapidly as we move away from the dominant eigenvector. Features 7 and 8 in Fig. 5 represent variations of the

eigenvalues in a small window about each pixel giving some textual information that is complementary to the corresponding pixel-based information. Eigenvector phase information is introduced by Features 9 and 10 for the two eigenvectors. The dominant eigenvector phase slope (Feature 9) is noisy except for the boats and land areas. The value on the boats is significantly higher than anywhere else. On land the eigenvector phase slope is very low, but very accurately determined as shown by Feature 5 (consistent with what is shown in Fig. 5 and the equations in Section II.C). Feature 9 benefits the class map generation by distinguishing boats from land and is not present for an amplitude-only situation. The second eigenvalue phase slope (Feature 10) highlights the surf region, where the secondary scattering mechanism displays velocity dependence.

B. SELECTING TRAINING DATA

Training data was generated using small regions of the image for each class as shown in Fig. 6. The size of class windows were chosen to be as small as possible while still capturing the essential variations in motion. The windows for boats are by necessity slightly smaller however boats have more compact motion variations. The total area of the training windows is kept small compared to the whole scene used for classification testing. These training regions are extracted from each of the 10 features and fed into the SVM classification learner.
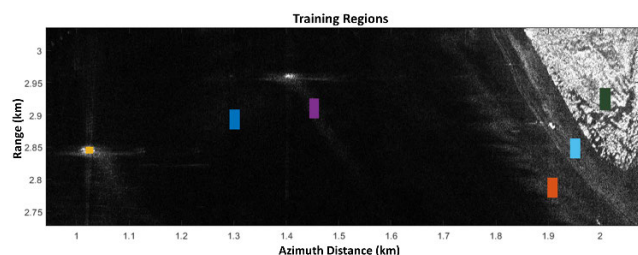

FIGURE 6. Regions used for classification training containing classes land, beach, surf, boat and their wakes.

C. CLASS MAP

We applied our image classification algorithm on the region of interest shown in Fig. 1, using the features shown in Fig. 5. For comparison we also produced classifications using the amplitude image and local standard deviation about each pixel (for some texture information). The resulting classification maps are shown in Fig. 7.

We observe that our algorithm does remarkably well at finding ambient, boat and land regions. It also does remarkably well in distinguishing beach region from land and water. Though the algorithm has some difficulty distinguishing different water disturbances (e.g. surf vs. wake), overall it renders an acceptable qualitative partitioning of these classes. Furthermore, repeating this process on a different set of eight phase centers using the first sets' training model gave virtually identical results (not shown), which further indicates the robustness of the approach.
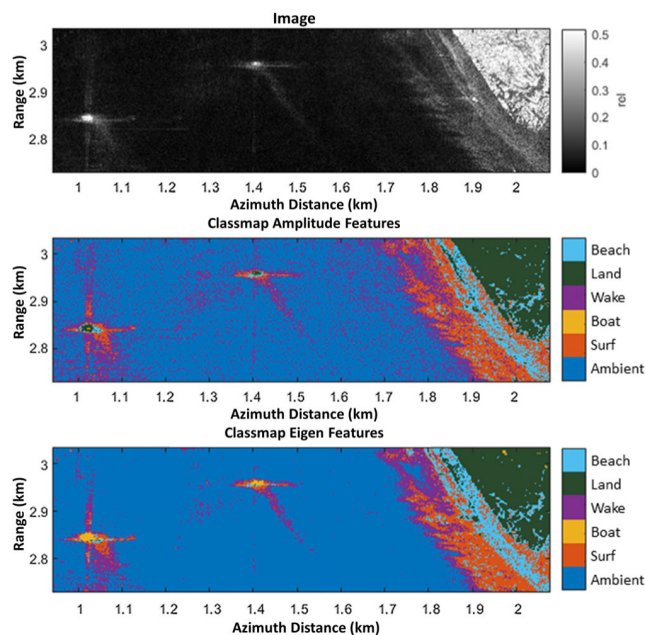

FIGURE 7. Image (top), amplitude-only classification map (middle) and MSAR eigen-feature derived classification map (bottom).

Fig. 7 shows a comparison between the amplitude derived classification map and the corresponding classification map derived from our MSAR based approach. We clearly see that the amplitude based approach does not distinguish land from boat since it has no direct access to velocity information (derived from the phases of the eigenvector components) as discussed in Section II. Furthermore the traditional amplitude based approach fails to detect the wake outside of the training box, and finally it fails to distinguish clearly the surf and beach classes in comparison to our MSAR based approach.

The percentage of correctly identify targets is plotted in Fig. 8. The MSAR-based approach (blue) provides a more accurate classification of the targets than the amplitude only classifier. The main differences between the two methods involve moving targets, i.e. ambient water, surf and boat, and to a lesser extent wakes and beaches. Only the land class is similarly identified by both methods. In fact, if the eigen features and amplitudes are combined to provide a super-set of classification features, the classification improvement over the MSAR feature classification is minimal, at best.

Our MSAR based classification algorithm is superior to the traditional approach to SAR based image classification in several respects. First, the selected features are well suited to physical interpretation of in-scene scattering mechanisms. The dominant eigenvector phases and their standard deviations contain information that characterizes scatterer motion. The ability to employ in-scene motion information is a unique aspect of our MSAR classification technique. The dominant eigenvalue contains image amplitude information, similar to that typically used in amplitude-only classifiers. As shown is Figs. 7 & 8, the results employing our classification features either with, or without, image amplitudes and standard
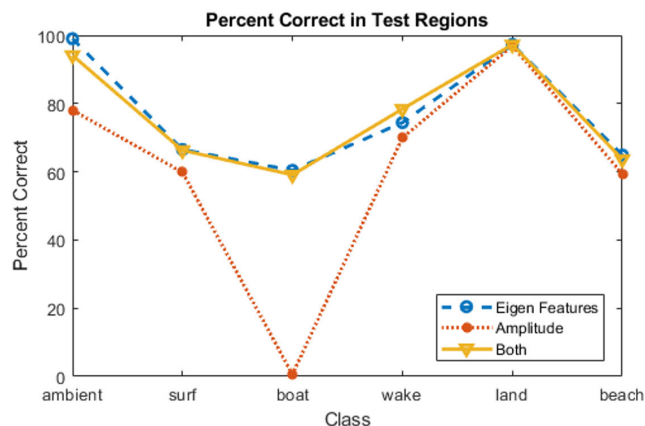
FIGURE 8. Percentage of pixels correctly classified within test regions.

deviations are equivalent. Second, overall the size of the training boxes is relatively small compared to the size of the scene i.e. we demonstrate excellent classification performance with limited training size. This feature renders our algorithm especially suitable for large-scale image classification problems. And, as pointed out earlier, classifiers trained on one set of MSAR channels and applied to an MSAR scene formed from a different, disjoint, set of channels produces very good classification results. Finally, the basic approach, eigen analysis of multi-channel covariance matrices, is easily extensible. Incorporating additional along-track channels merely increases the dimension of the covariance matrix; the analysis remains the same. Including cross-track channels changes the interpretation of the phases of the eigenvector components, but not the underlying methodology. Our techniques can therefore render high quality image classification when implemented in practical MSAR systems.

VI. CONCLUSION

In this paper, we describe a novel and robust classification procedure for maritime scenes using an MSAR system, which provides a powerful means of detecting motion in the scene. While previous research on MSAR data analysis has focused mainly on the imaging aspects, in this paper we demonstrate the power of MSAR based analysis for classification in maritime environments. Indeed our classification scheme is ideal for the maritime environment where every location is undergoing some form of motion.

We experimentally demonstrated, for the first time, the utility of our motion-based image classification algorithm using NRL MSAR imagery for a scene containing boats, wakes, surf, land, beach and ambient water classes. Our unique MSAR-based classification technique demonstrates great promise in separating these different motion classes.

We emphasize that our technique compliments previous approaches to image classification by exploiting motion information provided by the MSAR's unique along-track, multi-aperture configuration that is highly sensitive to in-scene velocities. In future work, our technique will be

extended to include height information via cross-track phase centers and sparsity approaches to improve practicality.

REFERENCES

[1] W. G. Carrara, R. S. Goodman, and R. M. Majewski, *Spotlight Synthetic Aperture Radar: Signal Processing Algorithms*. Boston, MA, USA: Artech House, 1995.

[2] C. V. Jakowatz, D. Wahl, P. Eichel, D. Ghiglia, and P. Thompson, *Spotlight-Mode Synthetic Aperture Radar: A Signal Processing Approach*. Boston, MA, USA: Kluwer, 1996.

[3] Y. Ding, N. Xue, and D. C. Munson, "An analysis of time-frequency methods in SAR imaging of moving targets," in *Proc. IEEE Sensor Array Multichannel Signal Process. Workshop. (SAM)*, Mar. 2000, pp. 222–225.

[4] P. R. Kersten, R. W. Jansen, K. Luc, and T. L. Ainsworth, "Motion analysis in SAR images of unfocused objects using time–frequency methods," *IEEE Geosci. Remote Sens. Lett.*, vol. 4, no. 4, pp. 527–531, Oct. 2007.

[5] R. W. Jansen, R. G. Raj, L. Rosenberg, and M. A. Sletten, "Practical multichannel SAR imaging in the maritime environment," *IEEE Trans. Geosci. Remote Sens.*, vol. 56, no. 7, pp. 4025–4036, Jul. 2018.

[6] R. Jansen, M. Sletten, and R. Raj, "Performance studies of emulated multi-channel SAR for motion characterization," *IEEE Trans. Aerosp. Electron. Syst.*, vol. 51, no. 4, pp. 3198–3209, Oct. 2015.

[7] R. G. Raj, R. W. Jansen, R. D. Lipps, M. A. Sletten, and L. Rosenberg, "Velocity-ISAR: On the application of ISAR techniques to multichannel SAR imaging," in *Proc. IEEE Radar Conf. (RadarCon)*, May 2015, pp. 1050–1055.

[8] M. A. Sletten, L. Rosenberg, S. Menk, J. V. Toporkov, and R. W. Jansen, "Maritime signature correction with the NRL multichannel SAR," *IEEE Trans. Geosci. Remote Sens.*, vol. 54, no. 11, pp. 6783–6790, Nov. 2016, doi: 10.1109/TGRS.2016.2590958.

[9] M. A. Sletten and J. V. Toporkov, "Improved ocean surface velocity precision using multi-channel SAR," *IEEE Trans. Geosci. Remote Sens.*, vol. 57, no. 11, pp. 8707–8718, Nov. 2019.

[10] M. A. Sletten, "Demonstration of SAR distortion correction using a ground-based multichannel SAR test bed," *IEEE Trans. Geosci. Remote Sens.*, vol. 51, no. 5, pp. 3181–3190, May 2013, doi: 10.1109/TGRS.2012.2212710.

[11] U. Srinivas, V. Monga, and R. G. Raj, "SAR automatic target recognition using discriminative graphical models," *IEEE Trans. Aerosp. Electron. Syst.*, vol. 50, no. 1, pp. 591–606, Jan. 2014.

[12] O. Kechagias-Stamatis and N. Aouf, "Fusing deep learning and sparse coding for SAR ATR," *IEEE Trans. Aerosp. Electron. Syst.*, vol. 55, no. 2, pp. 785–797, Apr. 2019.

[13] J. McKay, V. Monga, and R. G. Raj, "Robust sonar ATR through Bayesian pose-corrected sparse classification," *IEEE Trans. Geosci. Remote Sens.*, vol. 55, no. 10, pp. 5563–5576, Oct. 2017.

[14] Q. Zhao and J. C. Principe, "Support vector machines for SAR automatic target recognition," *IEEE Trans. Aerosp. Electron. Syst.*, vol. 37, no. 2, pp. 643–654, Apr. 2001.

[15] B. Bhanu and T. L. Jones, "Image understanding research for automatic target recognition," *IEEE Aerosp. Electron. Syst. Mag.*, vol. 8, no. 10, pp. 15–23, Oct. 1993.

[16] T. D. Ross, S. W. Worrell, V. J. Velten, J. C. Mossing, and M. L. Bryant, "Standard SAR ATR evaluation experiments using the MSTAR public release data set," *Proc. SPIE*, vol. 3370, pp. 566–573, Sep. 1998.

[17] C. Tison, N. Pourthie, and J.-C. Souyris, "Target recognition in SAR images with support vector machines (SVM)," in *Proc. IEEE Int. Geosci. Remote Sens. Symp.*, Jul. 2007, pp. 456–459.

[18] H. Bi, F. Xu, Z. Wei, Y. Xue, and Z. Xu, "An active deep learning approach for minimally supervised PolSAR image classification," *IEEE Trans. Geosci. Remote Sens.*, vol. 57, no. 11, pp. 9378–9395, Nov. 2019.

[19] H. Bi, J. Sun, and Z. Xu, "A graph-based semisupervised deep learning model for PolSAR image classification," *IEEE Trans. Geosci. Remote Sens.*, vol. 57, no. 4, pp. 2116–2132, Apr. 2019.

[20] F. Liu, Y. Duan, L. Li, L. Jiao, J. Wu, S. Yang, X. Zhang, and J. Yuan, "SAR image segmentation based on hierarchical visual semantic and adaptive neighborhood multinomial latent model," *IEEE Trans. Geosci. Remote Sens.*, vol. 54, no. 7, pp. 4287–4301, Jul. 2016.

[21] P. Zhang, M. Li, Y. Wu, and H. Li, "Hierarchical conditional random fields model for semisupervised SAR image segmentation," *IEEE Trans. Geosci. Remote Sens.*, vol. 53, no. 9, pp. 4933–4951, Sep. 2015.

[22] Y. Cao, H. Sun, and X. Xu, "An unsupervised segmentation method based on MPM for SAR images," *IEEE Geosci. Remote Sens. Lett.*, vol. 2, no. 1, pp. 55–58, Jan. 2005.

[23] F. A. Á. Rodrigues, J. F. S. R. Neto, R. C. P. Marques, F. N. S. de Medeiros, and J. S. Nobre, "SAR image segmentation using the roughness information," *IEEE Geosci. Remote Sens. Lett.*, vol. 13, no. 2, pp. 132–136, Feb. 2016.

[24] X. Tian, L. Jiao, L. Yi, K. Guo, and X. Zhang, "The image segmentation based on optimized spatial feature of superpixel," *J. Vis. Commun. Image Represent.*, vol. 26, pp. 146–160, Jan. 2015.

[25] J. Feng, Z. Cao, and Y. Pi, "Multiphase SAR image segmentation with G^0-statistical-model-based active contours," *IEEE Trans. Geosci. Remote Sens.*, vol. 51, no. 7, pp. 4190–4199, Jul. 2013.

[26] B. Huang, H. Li, and X. Huang, "A level set method for oil slick segmentation in SAR images," *Int. J. Remote Sens.*, vol. 26, no. 6, pp. 1145–1156, Mar. 2005.

[27] R. C. P. Marques, F. N. Medeiros, and J. S. Nobre, "SAR image segmentation based on level set approach and $\mathcal{G}_A^0$ model," *IEEE Trans. Pattern Anal. Mach. Intell.*, vol. 34, no. 10, pp. 2046–2057, Oct. 2012.

[28] J.-S. Lee and E. Pottier, *Polarimetric Radar Imaging: From Basics to Applications* (Optical Science and Engineering Book 143), 1st ed. Boca Raton, FL, USA: CRC Press, 2017.

[29] W. L. Melvin and A. J. Scheer, Eds., *Principles of Modern Radar: Advanced Techniques*. Edison, NJ, USA: SciTech, 2013.

[30] A. K. Jain, R. P. W. Duin, and J. Mao, "Statistical pattern recognition: A review," *IEEE Trans. Pattern Anal. Mach. Intell.*, vol. 22, no. 1, pp. 4–37, Jan. 2000.

MARK A. SLETTEN (Senior Member, IEEE) received the B.S., M.S., and Ph.D. degrees in electrical engineering from the University of Wisconsin–Madison, Madison, WI, USA, in 1984, 1987, and 1991, respectively. Since 1991, he has been with the U.S. Naval Research Laboratory, Washington, DC, USA, where he is involved in radar-based remote sensing research. This work includes the development of ultrawideband, polarimetric systems for determining the fundamental physics underlying low-grazing angle radar sea scatter, and the development and use of airborne radar systems (both real and synthetic aperture) for remote sensing of the coastal ocean. Past work has included a real-aperture radar study of the Chesapeake Bay outflow plume and the development of a lightweight, multiband, and interferometric SAR for use on a light aircraft. He has also conducted numerous field experiments that investigate the use of interferometric SAR systems for measuring ocean surface currents and mapping the space-time evolution of submesoscale oceanic eddies. This work included a collaborative effort with the University of Massachusetts at Amherst which demonstrated the use of dual-beam along-track SAR interferometry to measure vector ocean surface currents. He is currently involved in the development of multiphase-center synthetic aperture radar systems and algorithms for maritime surveillance and remote sensing. He received the 2014 Delores M. Etter Top Navy Scientists and Engineers of the Year Award.

THOMAS L. AINSWORTH (Fellow, IEEE) received the A.B. degree from Brown University, Providence, RI, USA, and the Ph.D. degree in theoretical physics from the State University of New York, Stony Brook, NY, USA. Since 1996, he has been a member of the Remote Sensing Division, U.S. Naval Research Laboratory (NRL), Washington, DC, USA. His research interest includes the analysis and novel applications of polarimetric and interferometric synthetic aperture radar (SAR) imagery, particularly geophysical parameter estimation using SAR polarimetry, polarimetric SAR calibration, polarimetric/interferometric image classification, and nonlinear approaches to data analysis. He is an Associate Editor of the IEEE Transactions on Geoscience and Remote Sensing.

ROBERT W. JANSEN (Member, IEEE) received the Ph.D. degree in theoretical physics from Arizona State University, Phoenix, in 1987. Over more than 30 years of research, he has tackled a broad range of problems in diverse fields, including semiconductor energetics, fluid dynamics, electromagnetic propagation, and sonar and RADAR imaging. In the last 25 years, his efforts have largely been focused in the area of synthetic aperture radar (SAR) and other remote sensing research, mostly as a part of the SEALAB Section of Code 7260 at the U.S. Naval Research Laboratory. He has made numerous significant contributions in areas that include SAR image enhancements, target identification, time-frequency exploitation, and near-shore wave, wind, and surf-zone modeling. He is currently engaged in the development of systems and processing schemes that provide motion measurement and maritime characterization using multichannel SAR (MSAR) techniques. He received the Alan Berman Publication Award, the Dr. Delores M. Etter Top Scientists and Engineers of the Year Award, and several technology transfer awards.

RAGHU G. RAJ (Senior Member, IEEE) received the Ph.D. degree in electrical engineering from The University of Texas at Austin, in 2007. He is currently a Senior Research Scientist and the Head of the Radar Division, Radar Imaging and Target ID Section, U.S. Naval Research Laboratory (NRL), Washington, DC, USA, where he leads the research and development of advanced methods in statistical signal processing and machine learning with applications to various U.S. DoD funded programs. He has over 60 publications in various international journals, conferences, and technical reports. He holds six U.S. patents. His research interests include signal/image processing and machine learning problems in radar and remote sensing. He was a recipient of the one NRL Alan Berman Publication Award.

• • •